Chemical Science

ROYAL SOCIETY OF CHEMISTRY

EDGE ARTICLE

View Article Online
View Journal | View Issue

Cite this: *Chem. Sci.*, 2024, **15**, 11053

All publication charges for this article have been paid for by the Royal Society of Chemistry

A record-high EQE of 7.65%@3300 cd m^{-2} achieved in non-doped near-ultraviolet OLEDs based on novel D′–D–A type bipolar fluorophores upon molecular configuration engineering†

Haoyuan Qi,[a] Danyu Xie,[b] Zexuan Gao,[a] Shengnan Wang,[a] Ling Peng,[c] Yuchao Liu,[a] Shian Ying,*[a] Dongge Ma*[b] and Shouke Yan*[ad]

Developing a high-performance near-ultraviolet (NUV) material and its simple non-doped device with a small efficiency roll-off and good color purity is a promising but challenging task. Here, we proposed a novel donor′–donor–acceptor (D′–D–A) type molecular strategy to largely solve the intrinsic contradictions among wide-bandgap NUV emission, fluorescence efficiency, carrier injection and transport. An efficient NUV fluorophore, **3,6-mPPICNC3**, exhibiting a hybridized local and charge-transfer state, is achieved through precise molecular configuration engineering, realizing similar hole and electron mobilities at both low and high electric fields. Moreover, the planarized intramolecular charge transfer excited state and steric hindrance effect endow **3,6-mPPICNC3** with a considerable luminous efficiency and good color purity in the aggregation state. Consequently, the non-doped device emitting stable NUV light with Commission Internationale de l'Eclairage (CIE) coordinates of (0.160, 0.032) and a narrow full width at half maximum of 44 nm exhibits a state-of-the-art external quantum efficiency (EQE) of 7.67% and negligible efficiency roll-off over a luminance range from 0 to 3300 cd m^{-2}. This is a record-high efficiency among all the reported non-doped NUV devices. Amazingly, an EQE of 7.85% and CIE coordinates of (0.161, 0.025) are achieved in the doped device. This demonstrates that the D′–D–A-type molecular structure has great potential for developing high-performance organic light-emitting materials and their optoelectronic applications.

Received 22nd April 2024
Accepted 13th June 2024

DOI: 10.1039/d4sc02655a

rsc.li/chemical-science

Introduction

Organic light-emitting diodes (OLEDs) have achieved large-scale commercial applications in full-color displays and solid-state lighting due to their unique advantages.[1–6] However, compared to red, green, and blue (RGB) OLEDs,[5,7–10] the development of near-ultraviolet (NUV) OLEDs with a Commission Internationale de l'Eclairage *y* coordinate (CIE*y*) below 0.035 is dropping noticeably behind. It's known that NUV emitters have broad application space and development prospects in the fields of optoelectronics, excitation light sources, high-density information storage, biological and medical applications.[11,12] Although some efforts have been made *via* rational molecular design or device engineering, external quantum efficiencies (EQEs) usually lie below 7% in simple non-doped NUV-OLEDs.[3,13–28] Moreover, most of the NUV-OLEDs suffer from serious efficiency roll-off at a high luminance level and poor color purity (the full width at half maximum (FWHM) value exceeding 50 nm), due to the intermolecular aggregation, strong intramolecular charge transfer (CT) effect, and unbalanced carrier injection, transport, and recombination.

For pursuing an efficient NUV material and its non-doped device, there are several aspects that need to be taken into thorough consideration during molecular design. First, the emitter should possess suitable molecular rigidity and an adequate molecular weight to ensure excellent thermal and morphological stabilities, thereby mitigating the impact of Joule heating on device degradation. Second, the molecular conjugation length and intermolecular aggregation effect must be carefully controlled to strike a balance between the NUV emission and photoluminescence (PL) efficiency. Additionally, the efficient utilization of electro-

[a]*Key Laboratory of Rubber-Plastics, Ministry of Education, School of Polymer Science and Engineering, Qingdao University of Science and Technology, Qingdao 266042, P. R. China. E-mail: shian0610@126.com*

[b]*Center for Aggregation-Induced Emission, Institute of Polymer Optoelectronic Materials and Devices, State Key Laboratory of Luminescent Materials and Devices, South China University of Technology, Guangzhou 510640, P. R. China. E-mail: msdgma@scut.edu.cn*

[c]*College of Chemistry and Chemical Engineering, Heze University, Heze 274015, P. R. China*

[d]*State Key Laboratory of Chemical Resource Engineering, College of Materials Science and Engineering, Beijing University of Chemical Technology, Beijing 100029, P. R. China. E-mail: skyan@mail.buct.edu.cn*

† Electronic supplementary information (ESI) available. See DOI: https://doi.org/10.1039/d4sc02655a

generated excitons is a crucial factor that affects the electroluminescence (EL) performance of NUV-OLEDs. Thermally activated delayed fluorescence (TADF) and noble-metal phosphorescent emitters can harvest both singlet and triplet excitons, achieving 100% exciton utilization efficiency (EUE).[1,29] However, it is virtually impossible to efficiently realize non-doped TADF or phosphorescent NUV-OLEDs with low efficiency roll-off due to the long exciton lifetimes and the principles of meticulous molecular design. A more prospective strategy is to construct NUV fluorophores with a hybridized local and charge-transfer (HLCT) excited state, which involves a high-lying reverse intersystem crossing (RISC) process that converts high-energy triplet excitons into singlet excitons, thereby facilitating the reutilization of triplet excitons. The efficient segregation of exciton conversion and radiation transition channels, coupled with the moderate strengths of donor/acceptor units, bestows HLCT emitters with both remarkable luminous efficiency and exceptional NUV emission capabilities.[30] Recently, most efficient HLCT-type NUV-OLEDs have been reported. For example, Li *et al.* realized a record-high maximum EQE of 11.3% and a high color purity EL peaking at 394 nm based on a doped emissive layer with an 8 wt% BO-biphenyl emitter.[31] Gan *et al.* reported a maximum EQE of 9.15% with the EL peak at 414 nm and a CIE*y* of 0.034 in the doped device with a doping concentration of 5 wt%.[26] Zhang *et al.* and Chen *et al.* realized maximum EQEs of 10.79% and 8.2% with CIE coordinates of (0.161, 0.031) and (0.161, 0.034) for carbazole-based emitters (2BuCzCNCz and POPCN-2CP) in the doped devices, while the EQEs were down to 5.24% and 7.5% with large FWHMs of 62 and 52 nm in the non-doped OLEDs.[32,33] Although the host–guest doping strategy can mitigate spectral redshift and enhance PL efficiency to a certain extent, such doped devices often face challenges such as potential phase separation issues, elevated processing costs, and the difficulty in selecting appropriate host materials. In previous work, we reported an efficient HLCT emitter (mP2MPC) *via* the *meta*-linkage pattern, achieving a maximum EQE of 6.09% with CIE coordinates of (0.163, 0.028) and a FWHM of 51 nm in the non-doped device.[34] Han *et al.* reported an emitter TPBCzC1 with a maximum EQE of 4.4% and a CIE*y* value of 0.035 in the non-doped OLED.[35] Until now, a record-breaking EQE of 7.5% with CIE coordinates (0.159, 0.035) and a FWHM of 52 nm has been achieved.[33] However, spectral broadening and the imbalance in hole/electron injection, transport, and recombination render non-doped NUV-OLEDs vulnerable to significant efficiency roll-off and compromised color purity.[13,36,37] Therefore, it is highly desirable and imperative to pursue a credible molecular design strategy that effectively addresses the aforementioned contradictions, thereby further promoting the advancement of non-doped NUV-OLEDs and their application at high luminance levels.

In this work, we proposed a feasible donor′–donor–acceptor (D′–D–A) type molecular design strategy to construct high-efficiency bipolar HLCT molecules with wide-bandgap emission. The above contradictions can be well reconciled by engineering molecular configuration precisely. As a result, the material 4-(6-(3-(1-phenyl-1*H*-phenanthro[9,10-*d*]imidazol-2-yl) phenyl)-9-propyl-9*H*-carbazol-3-yl)benzonitrile (**3,6-mPPICNC3**) exhibits remarkable fluorescence efficiencies in dispersion and aggregation states, as well as well-balanced hole and electron mobilities at both low and high electric fields. The non-doped OLED based on **3,6-mPPICNC3**, exhibiting a small CIE*y* value of 0.032, achieves a maximum EQE of 7.67%. Remarkably, it maintains a significant value of 7.65% at 3300 cd m^{-2}, showing negligible efficiency roll-off. This represents the state-of-the-art efficiency for non-doped NUV-OLEDs, particularly considering its CIE*y* value and minimal efficiency roll-off at such a high luminance level.

Results and discussion

Molecular design strategy and synthesis

A donor–acceptor (D–A) type emitter is a universal molecular paradigm to alleviate the problem of carrier injection and transport,[27,38–40] which can effectively broaden the exciton recombination zone, and further suppress exciton quenching. Additionally, it has been proven that a D–A type emitter with the intramolecular CT effect can enhance the utilization of triplet excitons by the RISC process, such as the TADF and HLCT mechanism. However, the strong intramolecular CT effect would also trigger phenomena such as bathochromic shift of emission, inferior color purity and reduced overlap of molecular frontier orbitals (resulting in low fluorescence efficiency) to a certain extent. Several successful strategies have been proposed to weaken this effect for exploiting D–A-type NUV emitters, for example, incorporating a steric group, introducing a twisted bridge, and utilizing weak electron-donating/accepting groups. Based on these strategies, a series of D–(π)–A type,[41] donor–acceptor–donor (D–A–D) type,[42–45] acceptor–donor–acceptor (A–D–A) type,[46] and donor′–acceptor–donor (D′–A–D) type wide-bandgap organic emitters were reported in doped OLEDs (Fig. 1).[47] Nevertheless, non-doped NUV-OLEDs still display unsatisfactory EL performance. Here, we proclaim a promising and novel D′–D–A-type molecular design strategy to address the abovementioned contradictions, where *N*-propyl-modified carbazole (C3Cz) with the exceptional merits of hole transport ability and good thermal stability was selected as a rigid bridged donor;[48–52] benzonitrile (PhCN) was selected as an acceptor that may enhance supramolecular interactions in the neat film;[53–56] a 1,2-diphenyl-1*H*-phenanthro[9,10-*d*]imidazole (PPI) chromophore with a low T_1 energy level, good thermal stability and high fluorescent efficiency was selected as a second donor group,[57–60] which is linked to the C3Cz donor through a single bond. Such D′–D–A type molecular geometry endows the emitters with planarized intramolecular charge transfer (PLICT) state characteristics, maintaining high photoluminescence quantum yields (PLQYs) in dispersion and aggregation states.[61,62] Meanwhile, efficient NUV emission as well as balanced bipolar transport are achieved by precisely modulating molecular configuration engineering, that is regulating substitution modes onto C3Cz (3, 6 or 2, 7) and the substitution positions of PPI (*meta*- or *para*-position).

Accordingly, four isomers, namely 4-(7-(3-(1-phenyl-1*H*-phenanthro[9,10-*d*]imidazol-2-yl)phenyl)-9-propyl-9*H*-carbazol-2-yl) benzonitrile (**2,7-mPPICNC3**) and 4-(7-(4-(1-phenyl-1*H*-phenanthro[9,10-*d*]imidazol-2-yl)phenyl)-9-propyl-9*H*-carbazol-2-yl) benzonitrile (**2,7-pPPICNC3**), 4-(6-(4-(1-phenyl-1*H*-phenanthro

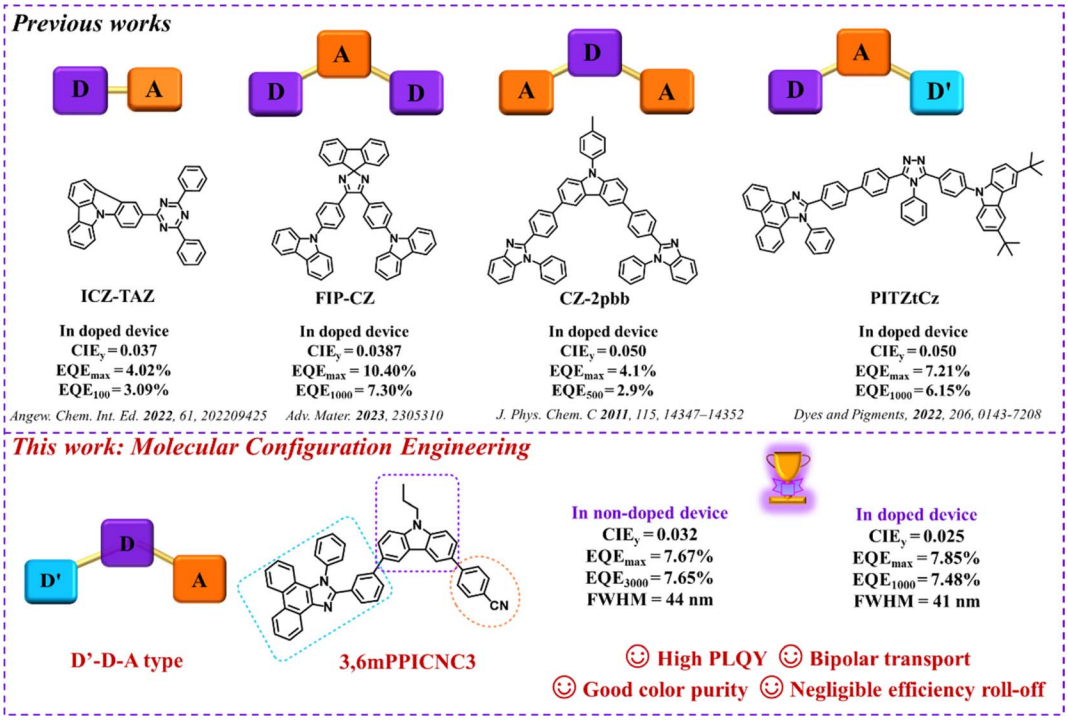

Fig. 1 The reported emitters with different D–A structures and the molecular design strategy of this work.

[9,10-*d*]imidazol-2-yl)phenyl)-9-propyl-9*H*-carbazol-3-yl) benzonitrile (**3,6-pPPICNC3**), and **3,6-mPPICNC3** were designed and facilely synthesized (Schemes S1–S3†). The detailed synthesis method and structural characterization are described in the ESI.† According to the thermogravimetric analysis and differential scanning calorimetry measurements (Fig. S1†), high decomposition temperatures (T_d, 5% weight loss) of 439, 495, 492, and 459 °C are achieved for **3,6-mPPICNC3**, **3,6-pPPICNC3**, **2,7-mPPICNC3**, and **2,7-pPPICNC3**, respectively. The glass transition temperature (T_g) was determined to be 143 °C for **2,7-mPPICNC3**, while no T_gs were observed for other emitters in the temperature range of 25–300 °C (Fig. S2†). In addition, the surface morphology and PL spectrum of the vacuum-sublimed film were almost unchanged after exposed to the ultraviolet lamp for 24 h (Fig. S3†). These results indicate that all the isomers have excellent thermostability and photostability, which is desired for improving the efficiency and lifetime of OLEDs. As shown in Fig. S4,† the oxidation potentials were determined to be 0.896, 0.853, 0.896 and 0.867 V, referring to the highest occupied molecular orbital (HOMO) energy levels of −5.20, −5.17, −5.16 and −5.18 eV for **3,6-mPPICNC3**, **3,6-pPPICNC3**, **2,7-mPPICNC3**, and **2,7-pPPICNC3**. Lowest unoccupied molecular orbital (LUMO) energy levels can be calculated to be −1.87, −2.01, −1.90 and −2.12 eV, according to the differences between HOMOs and optical bandgaps (E_gs).

Theoretical calculations

The optimization of geometrical configurations, frontier molecular orbital (FMO) distributions of **3,6-mPPICNC3**, **3,6-pPPICNC3**, **2,7-mPPICNC3**, and **2,7-pPPICNC3**, and their building units was performed by density functional theory (DFT) calculations at the B3LYP/6-31G(d,p) basis set. As shown in Fig. S5,† there exist limited HOMO distributions on the C2 and C7 atoms of the C3Cz unit and *meta*-position C atom of the PPI group, signifying that the conjugation interaction among building units can be well controlled by the molecular configuration engineering. It can be seen in Fig. 2 that all the emitters show moderately distorted molecular conformation with D–A dihedral angles (θ_1s) of 35.99–36.43°, twist angles (θ_2s) of 33.36–36.30° between C3Cz and the connected benzene of the PPI unit, and twist angles (θ_3s) of 19.71–30.02° between imidazole and connected benzene. The HOMO distributions are mainly limited to the additional donor PPI for **3,6-mPPICNC3** and **2,7-mPPICNC3**, while they are further slightly extended to the adjacent C3Cz group in the molecules **3,6-pPPICNC3** and **2,7-pPPICNC3**. The LUMOs of **3,6-mPPICNC3** and **3,6-pPPICNC3** were mostly distributed on the PhCN segment with minor contribution from the donor-bridge C3Cz, while those are exclusively located on the whole PhCN and central carbazole and a residual on the adjacent benzene ring in the case of **2,7-mPPICNC3** and **2,7-pPPICNC3**. Consequently, **3,6-mPPICNC3** and **2,7-pPPICNC3** show the widest and least energy gaps of 3.62 and 3.40 eV, respectively.

In order to investigate the excited state properties of all the emitters, the optimization of the geometry of the lowest singlet (S_1) excited state and natural transition orbital (NTO) analysis were carried out. The variations of geometric configuration between the ground (S_0) state and S_1 state are shown in Fig. 2. The dihedral angles (θ_1, θ_2, and θ_3) in the S_1 state

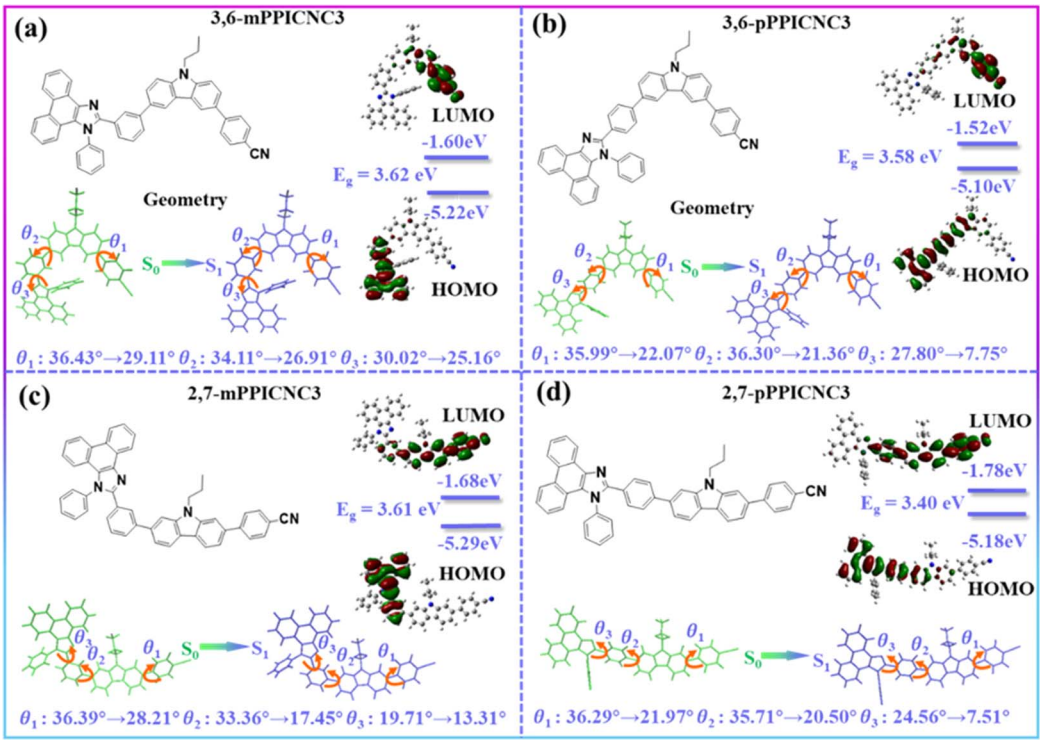

Fig. 2 Chemical structures, optimized geometry configurations of ground states and singlet states and FMO distributions for (a) **3,6-mPPICNC3**, (b) **3,6-pPPICNC3**, (c) **2,7-mPPICNC3**, and (d) **2,7-pPPICNC3**.

become smaller, which decrease from 36.43°, 34.11° and 30.02° to 29.11°, 26.91° and 25.16° for **3,6-mPPICNC3**, from 35.99°, 36.30° and 27.80° to 22.07°, 21.36° and 7.75° for **3,6-pPPICNC3**, from 36.39°, 33.36° and 19.71° to 28.21°, 17.45 and 13.31° for **2,7-mPPICNC3**, and from 36.29°, 35.71° and 24.56° to 21.97°, 20.50° and 7.51° for **2,7-pPPICNC3**, respectively. Such a phenomenon demonstrates that all the emitters possess the PLICT features in the excited state exactly.[45,61,63,64] In addition, as shown in Table S1,† the bond lengths (L_1, L_2 and L_3) between C3Cz and PhCN (PPI) units are shortened from S_0 to S_1 geometries for all the emitters. Taking **3,6-mPPICNC3** as an example, L_1, L_2 and L_3 are calculated as 1.477, 1.481 and 1.467 Å for the S_0 geometry, which reduce to 1.455, 1.476 and 1.450 Å in the S_1 geometry. This result provides a new proof for the existence of the PLICT process. As shown in Tables S2–S5,† there are some scale of orbital overlap on the carbazole group for **3,6-mPPICNC3** and on the benzene ring of the PPI unit for **2,7-mPPICNC3** in the $S_0 \rightarrow S_1$ transition, while a large orbital separation exists between hole and particle distributions, belonging to CT-dominated HLCT excited states. In the $S_0 \rightarrow S_2$ transition, **3,6-mPPICNC3** and **2,7-mPPICNC3** show archetypal HLCT excited states with the hole and particle undergoing partial separation and partial overlap. The $S_0 \rightarrow S_1$ transitions for **3,6-pPPICNC3** and **2,7-pPPICNC3** with the *para*-substitution of the PPI group can be considered as typical HLCT states, where the hole and particle distributions show large overlaps in the carbazole and benzene component of PPI, and effective separation in the second donor and acceptor segments. This endows them with higher oscillator strengths than that of the isomers with *meta*-substitution of the PPI group. As shown in Tables S6 and S7,† the calculated S_1 and T_1 energy levels are 3.343 and 2.710 eV for **3,6-mPPICNC3**, 3.285 and 2.606 eV for **3,6-pPPICNC3**, 3.343 and 2.626 eV for **2,7-mPPICNC3**, and 3.107 and 2.506 eV for **2,7-pPPICNC3**, respectively, corresponding to the energy splittings (ΔE_{ST}s) between S_1 and T_1 of 0.633, 0.679, 0.717 and 0.601 eV, excluding the TADF process. As for **3,6-mPPICNC3**, the high-lying triplet states (T_4, T_5 and T_6) show obvious HLCT, locally excited (LE) and HLCT states, which show smaller energy differences (0.0173, 0.115 and 0.004 eV) and larger spin–orbit coupling (SOC) values (0.147, 0.128 and 0.059 cm^{-1}) with the S_1 state. This revelation indicates that it could facilitate multi-channel high-lying RISC processes, according to Fermi's golden and El-Sayed rules (Fig. S6†).[65,66] Correlation analysis of other isomers is shown in the ESI.†

Photophysical properties

The absorption and PL spectra of **3,6-mPPICNC3**, **3,6-pPPICNC3**, **2,7-mPPICNC3** and **2,7-pPPICNC3** in dilute toluene solution are illustrated in Fig. 3a. The absorption peaks at around 285 and 305 nm can be attributed to the absorption of the carbazole unit, while the absorption band in the range of 325–365 nm may be ascribed to the π–π* transition of the PPI unit.[67] It is worth noting that low-energy bands were observed at different positions for the isomers, resulting from varying

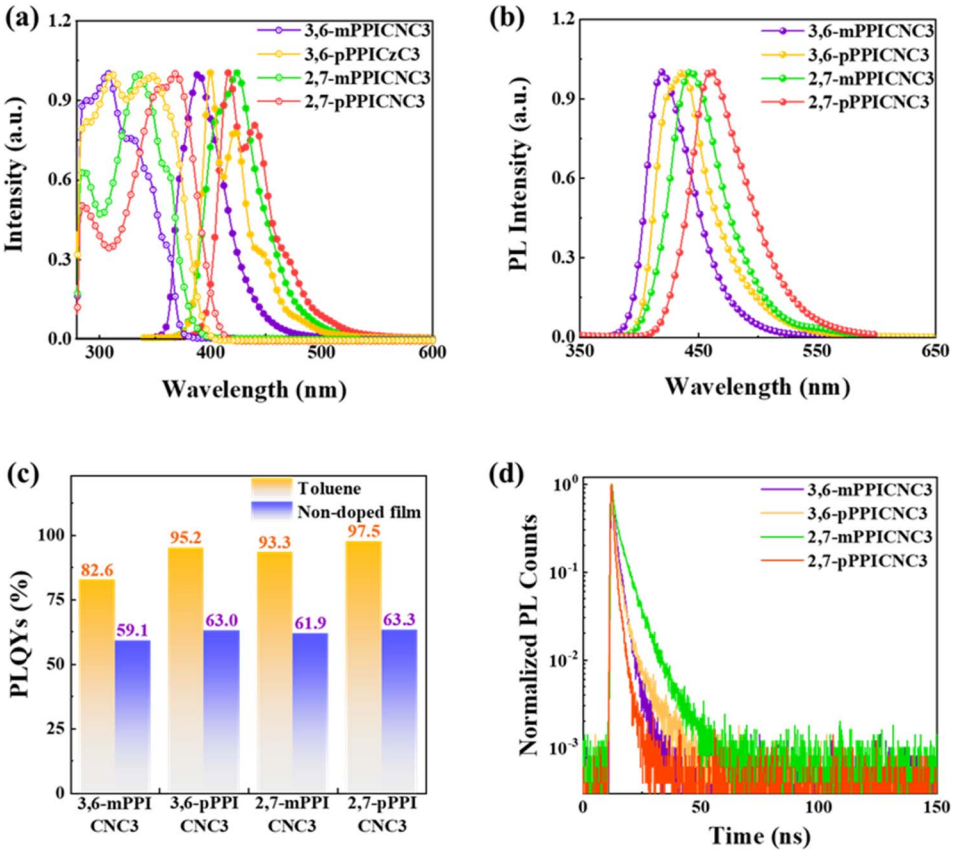

Fig. 3 (a) Normalized absorption and PL spectra of **3,6-mPPICNC3**, **3,6-pPPICNC3**, **2,7-mPPICNC3** and **2,7-pPPICNC3** in toluene solution (10^{-5} M). (b) Normalized PL spectra in the neat film. (c) PLQYs in toluene and the neat film. (d) Transient PL decay spectra in the neat film.

degrees of π-conjugation expansion, which is highly dependent on the positions of attachment of A and D′ units to the C3Cz donor. According to the onset of absorption spectra, the values of E_g can be estimated to be 3.33, 3.16, 3.26 and 3.06 eV for **3,6-mPPICNC3**, **3,6-pPPICNC3**, **2,7-mPPICNC3** and **2,7-pPPICNC3**, respectively. It can be seen from PL spectra that all the compounds are emitted in the NUV to deep-blue light region with the maximum peaks of 389, 400, 424 and 417 nm, corresponding to PL quantum yields (PLQYs) of 82.6%, 95.2%, 93.3% and 97.5%, respectively (Fig. 3c). Moreover, the PL spectra of **3,6-mPPICNC3** and **2,7-mPPICNC3** with the *meta*-linkage of PPI exhibit structureless profiles, while those of **3,6-pPPICNC3** and **2,7-pPPICNC3** with the *para*-linkage of PPI feature distinct vibronic fine structures. The PL peaks of the neat films exhibit a certain degree of bathochromic-shifts at 419, 437, 443 and 460 nm with the related FWHMs of 45, 50, 51 and 55 nm, corresponding to the PLQYs of 59.1%, 63.0%, 61.9% and 63.3% for **3,6-mPPICNC3**, **3,6-pPPICNC3**, **2,7-mPPICNC3** and **2,7-pPPICNC3**, respectively (Fig. 3b and c). Notably, such high PLQY values achieved in neat films are higher than those of most reported HLCT emitters.[58,68–72] By comparison with other isomers, **3,6-mPPICNC3** exhibits a blue-shift with higher color purity, which can be attributed to the rigid configuration and large steric hindrance effect that can effectively suppress the structure relaxation and intermolecular aggregation. The doped film with a 5 wt% emitter dispersed into polar poly(methyl methacrylate) (PMMA) exhibits blue-shifted PL peaks of 399, 425, 422 and 443 nm, with the enhanced PLQYs of 61.4%, 93.4%, 91.0% and 97.4% (Fig. S7†). Table 1 summarizes the photophysical and electrochemical parameters of the four isomers.

Low-temperature fluorescence and phosphorescence spectra at 77 K in toluene solution were measured to estimate the S_1 and T_1 energy levels (Fig. S8†). According to the emission peaks, the ΔE_{ST}s can be calculated to be 0.63, 0.67, 0.56, and 0.54 eV for **3,6-mPPICNC3**, **3,6-pPPICNC3**, **2,7-mPPICNC3** and **2,7-pPPICNC3**, respectively (Table 1). Moreover, transient PL decay curves in solutions and films show single-exponential fluorescence lifetimes in the nanosecond range (Fig. 3d, S9, S10 and Table S8†), which further illustrates that the TADF process can be ruled out. Due to the rapid RISC process from high-lying triplet states to S_1, the delayed lifetimes and RISC rates cannot be obtained.[30] Based on the PLQYs and decay lifetimes, the radiative and non-radiative rates (k_r and k_{nr}) were calculated (Table S8†). All four emitters show outstanding k_r values exceeding 1.9×10^8 s^{-1}, which would inhibit the exciton annihilation effects and ameliorate the efficiency roll-off in the OLEDs. The emitters with *para*-connection between the D′ and D units show higher k_rs as a result of the increased FMO overlaps. Specifically, the PLQYs were improved with the increase of

Table 1 The photophysical and electrochemical parameters of the emitters

	Solution[a]			Neat film[b]				
Compounds	λ_{Abs} [nm]	λ_{Fluo} [nm]	Φ_{PL} [%]	λ_{Fluo} [nm]	Φ_{PL} [%]	FWHM [nm eV^{-1}]	HOMO/LUMO/E_g[c] [eV]	$E_{S_1}/E_{T_1}/\Delta E_{ST}$[d] [eV]
3,6-mPPICNC3	286,307 361	389	82.6	419	59.1	45/0.308	−5.20/−1.87/3.33	3.16/2.53/0.63
3,6-pPPICNC3	284,310 348	400 422(sh)	95.2	437	63.0	50/0.326	−5.17/−2.01/3.16	3.10/2.43/0.67
2,7-mPPICNC3	285,334 362	407(sh),424	93.3	443	61.9	51/0.315	−5.16/−1.90/3.26	2.98/2.42/0.56
2,7-pPPICNC3	285,354 368	417 441(sh)	97.5	460	63.3	55/0.350	−5.18/−2.12/3.06	2.96/2.42/0.54

[a] Measured in toluene solution (10^{-5} M) at 300 K. [b] Measured in non-doped films at 300 K. [c] HOMO energy level: obtained from CV measurement. E_g: calculated from the absorption onset in toluene solution. LUMO energy level: calculated by $E_{LUMO} = E_{HOMO} + E_g$. [d] Estimated by the peaks of low-temperature fluorescence and phosphorescence spectra at 77 K, $\Delta E_{ST} = E_{S_1} - E_{T_1}$.

solvent polarity (Table S9†), which is consistent with the PLICT process.[22,63]

To further investigate the excited state properties, solvatochromic effects were measured in various solvents. It is found that the absorption spectra show nearly no changes with increasing solvent polarity (Fig. S11†), while their PL spectra exhibit significant redshifts as the solvent polarity increases (Fig. 4 and S12–S14†). All the emitters display clear vibronic fine structures in the low polar *n*-hexane solvent. As the solvent polarity increases, the emitters **3,6-mPPICNC3** and **2,7-mPPICNC3** gradually exhibit structureless and broadened PL emission, corresponding to a larger red-shift of 65 and 23 nm. In contrast, the PL spectra of **3,6-pPPICNC3** and **2,7-pPPICNC3** in the highly polar acetonitrile solvent display weak vibrational fine structure, illustrating that their S_1 states hold more LE component than those of **3,6-mPPICNC3** and **2,7-mPPICNC3**, agreeing well with the theoretical calculations. As was investigated through the analysis of Stokes shift *versus* solvent orientation polarizability curves by the Lippert–Mataga solvatochromic model, the two-segment linear relationship can be observed for **3,6-mPPICNC3** and **2,7-pPPICNC3**, representing typical HLCT states.[3,30] **3,6-pPPICNC3** and **2,7-mPPICNC3** display linear relationships with excited state dipole moments of 10.45 and 11.47 debye, signifying that there exists only one excited state in different polar solvents, belonging to the quasi-equivalent HLCT states.[54,70,73] This also was supported by the single-component nanosecond-scale fluorescence lifetimes and high PLQYs in both low and high polar solvents. These results indicate that all the emitters could achieve the reutilization of inactivated triplet excitons and enable the realization of high-efficiency non-doped OLEDs.

Bipolar transport properties

The bipolar transport ability is one of the key factors contributing to efficiency roll-off in non-doped OLEDs. In order to evaluate it, single-carrier devices were fabricated with the configurations of [indium-tin-oxide (ITO)/1,3,5-tris(1-phenyl-1*H*-benzo[*d*]imidazol-2-yl)benzene (TPBi, 10 nm)/emitters (80 nm)/TPBi (10 nm)/LiF (1 nm)/Al (100 nm)] for the electron-only devices (EODs) and [ITO/N^4,N$^{4'}$-di(naphthalen-1-yl)-N^4,N$^{4'}$-diphenyl-[1,1′-biphenyl]-4,4′-diamine (NPB, 10 nm)/emitters (80 nm)/NPB (10 nm)/Al (100 nm)] for hole-only devices (HODs). According to the space-limited-current (SCLC) method, which can be described by the Mott–Gurney eqn (1):[74]

$$J = \frac{9}{8}\varepsilon_0\varepsilon_r\mu\frac{E^2}{L} \quad (1)$$

Here, J is the current density, ε_0 represents the vacuum permittivity ($\varepsilon_0 = 8.85 \times 10^{-14}$ C V^{-1} cm^{-1}), ε_r stands for the relative dielectric constant, which is considered to be 3.0 for the

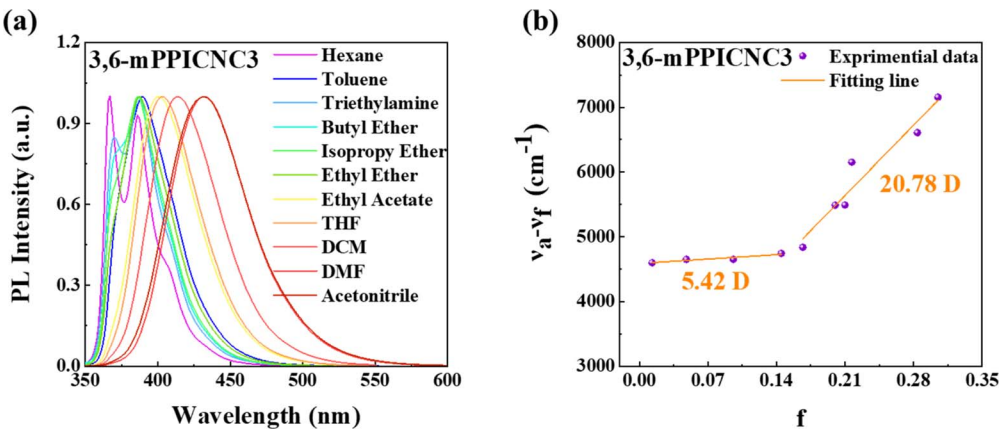

Fig. 4 Solvation effects on PL spectra (a) and Lippert–Mataga plots (b) for **3,6-mPPICNC3**.

organic semiconductor, μ represents the carrier mobility, E is the electric field intensity, and L means the thickness of the emitters. In view of the effect of energetic disorder on carrier mobility, the mobility dependent on the electric field can be expressed by a Poole–Frenkel equation:

$$\mu = \mu_0 e^{-\gamma\sqrt{E}} \quad (2)$$

Here, μ_0 is the zero-field mobility and γ is the Poole–Frenkel factor. Thus, the field-dependent SCLC can be expressed as:

$$J = \frac{9}{8}\varepsilon_0\varepsilon_r\mu_0\frac{V^2}{L^3}e^{0.891\gamma\sqrt{\frac{V}{L}}} \quad (3)$$

It can be seen in Fig. S15† that the HODs and EODs produce significant hole or electron currents as the applied voltages increase, indicating that all the isomers exhibit a considerable bipolar transport nature. As shown in Fig. 5, substitution positions of the PPI unit have a slight effect on the electron mobility whereas the hole mobilities of *para*-isomers are superior to those of *meta*-isomers. In addition, compared to the 3,6-substitution mode on C3Cz, the 2,7-substitution mode decreases the hole mobility of emitters but enhances the electron mobility, attributed to deeper HOMO energy levels and more planarized molecule structures. Consequently, the electron mobility decreases in the order **2,7-pPPICNC3** (2.83×10^{-5} cm^2 V^{-1} s^{-1}) > **2,7-mPPICNC3** (2.23×10^{-5} cm^2 V^{-1} s^{-1}) > **3,6-pPPICNC3** (2.97×10^{-6} cm^2 V^{-1} s^{-1}) > **3,6-mPPICNC3** (1.52×10^{-6} cm^2 V^{-1} s^{-1}) at an electric field of 5×10^5 V cm^{-1}, while the hole mobility decreases in the order **3,6-pPPICNC3** (4.26×10^{-5} cm^2 V^{-1} s^{-1}) > **2,7-pPPICNC3** (1.47×10^{-5} cm^2 V^{-1} s^{-1}) > **3,6-mPPICNC3** (2.28×10^{-6} cm^2 V^{-1} s^{-1}) > **2,7-mPPICNC3** (6.15×10^{-7} cm^2 V^{-1} s^{-1}), respectively. It should be noted that **3,6-mPPICNC3** exhibits more balanced electron and hole mobilities in both low and high electric fields, which can effectively suppress the exciton-polaron quenching effect, thereby resulting in a low efficiency roll-off at high current densities.

EL performance

Considering their high PLQYs and excellent bipolar transport properties, we further investigated the EL performance of non-doped devices with the four emitters as pure emissive layers, utilizing the optimized device configurations of ITO/1,4,5,8,9,11-hexaazatriphenylenehexacarbonitrile (HATCN, 20 nm)/4,4′-(cyclohexane-1,1-diyl)bis(*N*,*N*-di-*p*-tolylaniline) (TAPC, 45 nm)/tris(4-(9*H*-carbazol-9-yl)phenyl)amine (TCTA)

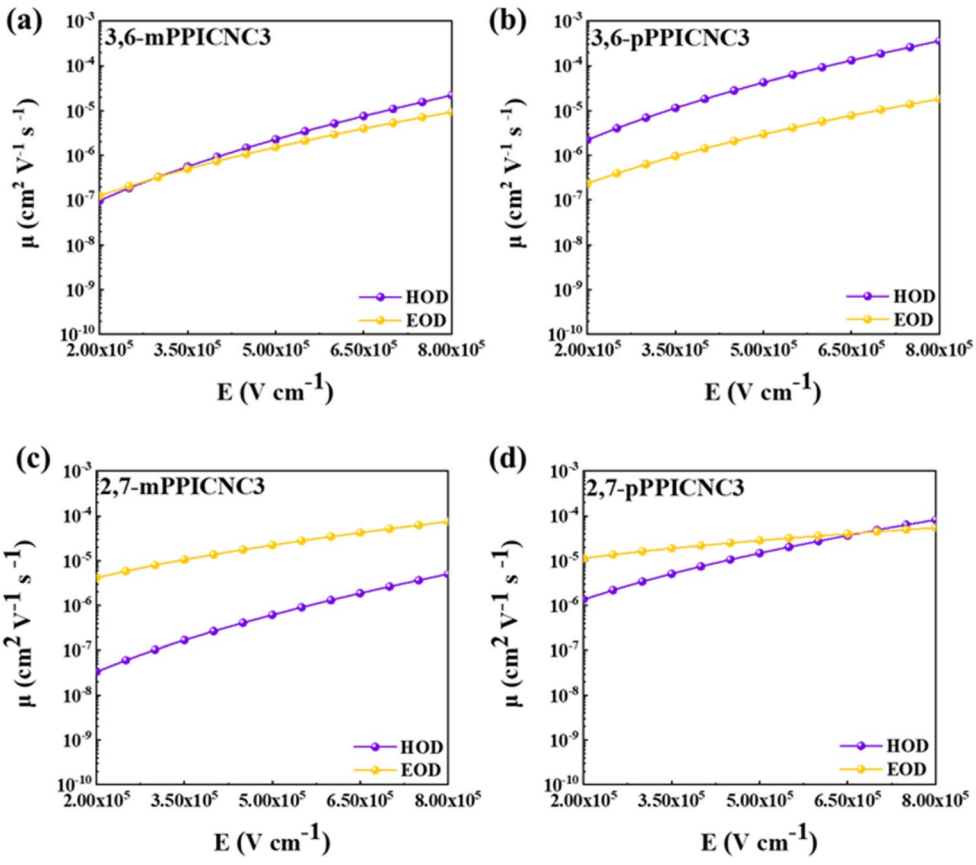

Fig. 5 Hole and electron mobilities *versus* electric field curves for (a) 3,6-mPPICNC3, (b) 3,6-pPPICNC3, (c) 2,7-mPPICNC3 and (d) 2,7-pPPICNC3.

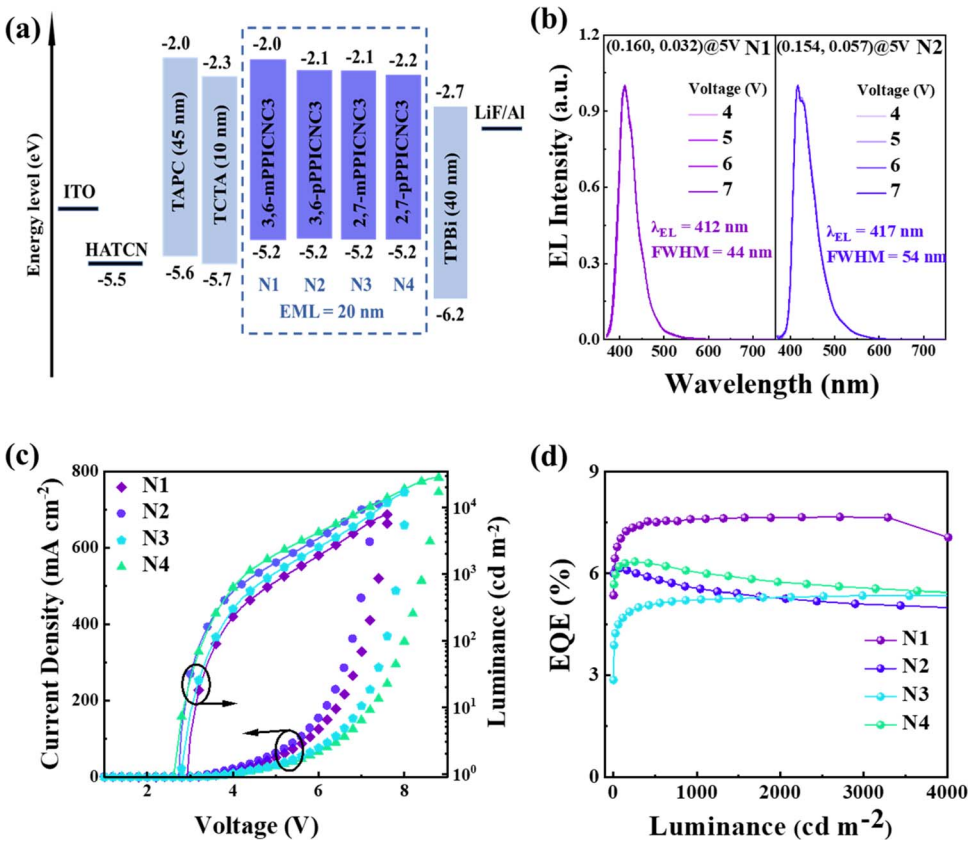

Fig. 6 (a) Device structures and energy level diagrams of the devices **N1–4**. (b) Normalized EL spectra at different applied voltages of the devices **N1** and **N2**. (c) Current density–voltage–luminance curves of the devices **N1–4**. (d) EQEs *versus* luminance curves of the devices **N1–4**.

(10 nm)/emissive layer (20 nm)/TPBi (10 nm)/LiF (1 nm)/Al (100 nm). Here, the emissive layers of devices (**N1, N2, N3** and **N4**) correspond to **3,6-mPPICNC3**, **3,6-pPPICNC3**, **2,7-mPPICNC3** and **2,7-pPPICNC3**; HATCN, LiF, TAPC, TCTA, and TPBi served as hole-injection, electron-injection, hole-transport, exciton-blocking, and electron-transport layers, respectively. The relevant organic molecular structures, energy level diagrams and EL performance of the devices are shown in Fig. 6 and S16–S18,† and the corresponding values are listed in Table 2. As expected, the device **N1** with **3,6-mPPICNC3** as the pure emissive layer displays a stable NUV emission with good color purity, corresponding to the CIE coordinates of (0.162, 0.032) and the FWHM value of 44 nm (0.313 eV). Additionally, devices **N2–4**, based on **3,6-pPPICNC3**, **2,7-mPPICNC3** and **2,7-pPPICNC3**, respectively, show red-shifted and slightly broadening emissions located in deep-blue and blue light regions, having CIE coordinates of (0.154, 0.057), (0.155, 0.075), and (0.158, 0.141), respectively. Notably, devices **N1–4** exhibit low turn-on voltages ranging from 2.7 to 2.9 V due to the well matched energy level arrangement and bipolar transport ability of the emitters which facilitate effective carrier injection, transport and recombination. The maximum luminance, current efficiency, power efficiency and EQE of 7844 cd cm^{-2}, 1.52 cd A^{-1}, 1.35 lm W^{-1} and 7.67% are achieved simultaneously in the device **N1**. In particular, the EQE of device **N1** remains extraordinarily high at 7.65% even at a high luminance of 3300 cd m^{-2}, demonstrating negligible efficiency roll-off. This can be attributed to the rapid k_r value and balanced bipolar property of **3,6-mPPICNC3**. Meanwhile, devices **N2–4** achieve the maximum EQE values of 6.16%, 5.39%, and 6.35%, and maintain EQE levels of 5.56%, 5.23% and 6.05% at 1000 cd m^{-2}, respectively. The EL performance of device **N3** based on **2,7-mPPICNC3** is unsatisfactory compared to the other devices. This can be attributed to its long fluorescence lifetime and imbalanced hole/electron mobilities. Here, we define J_{90} as the current density at which the EQE falls to 90% of its peak value, as a means of assessing efficiency roll-off. In this context, a high J_{90} value indicates a low efficiency roll-off. The J_{90}s of non-doped devices **N1–4** can be extracted to be 327, 41, 486, and 31 mA cm^{-2}, respectively. Such superior values achieved in the devices **N1** and **N3** with **3,6-pPPICNC3** and **2,7-mPPICNC3** as emitters surpass those of most traditional fluorescent OLEDs.[29]

The EUE of OLEDs can be described by eqn (4):

$$\mathrm{EUE} = \frac{\mathrm{EQE}}{\gamma \times \Phi_{\mathrm{PL}} \times \eta_{\mathrm{OUT}}} \quad (4)$$

Here, γ is the recombination efficiency of the injected holes and electrons (ideally 100%), η_{OUT} is the light out coupling efficiency

Table 2 Summary of key EL parameters for the devices

Devices	EML	$V_{on/1000}$ [a] [V]	Luminance$_{max}$ [d] [cd m^{-2}]	$CE_{max/1000}$ [b] [cd A^{-1}]	$PE_{max/1000}$ [b] [lm W^{-1}]<	$EQE_{max/1000}$ [b] [%]	E_{UE} [c] [%]	λ_{EL} [e] [nm]	FWHM [e] [nm eV^{-1}]	CIE(x, y) [e]
N1	**3,6-mPPICNC3**	2.9/5.3	7844	1.52/1.52	1.35/0.88	7.67/–/7.65[f]	64.9–43.3	412	44/0.313	(0.160, 0.032)
N2	**3,6-pPPICNC3**	2.7/4.6	11 197	2.96/2.52	3.32/1.72	6.16/5.56	48.9–32.6	417	54/0.362	(0.154, 0.057)
N3	**2,7-mPPICNC3**	2.8/5.0	16 922	3.35/3.32	2.76/2.09	5.39/5.23	43.5–29.0	430	58/0.373	(0.155, 0.075)
N4	**2,7-pPPICNC3**	2.7/4.3	28 073	7.72/7.25	8.09/5.30	6.35/6.05	50.2–33.4	455	64/0.387	(0.158, 0.141)
D1	**CBP:3,6-mPPICNC3**	3.4/7.2	3058	0.73/0.71	0.32/0.29	7.85/7.48	63.9–42.6	391	41/0.321	(0.161, 0.025)
D2	**CBP:3,6-pPPICNC3**	3.2/6.2	4469	1.53/1.44	1.30/0.73	7.51/6.85	40.2–26.8	406	41/0.293	(0.160, 0.035)
D3	**CBP:2,7-mPPICNC3**	3.3/6.9	3847	1.15/1.08	0.98/0.49	5.42/4.97	29.8–19.9	425	51/0.361	(0.161, 0.033)
D4	**CBP:2,7-pPPICNC3**	3.1/5.4	9355	3.51/3.28	3.43/1.91	6.47/6.05	33.2–22.1	426	47/0.313	(0.156, 0.063)

[a] Measured at 1 and 1000 cd m^{-2}. [b] Maximum efficiencies and the values taken at 1000 cd m^{-2}. [c] Exciton utilization efficiency. [d] Maximum luminance. [e] Measured at a voltage of 5 V. [f] EQE at 3300 cd cm^{-2}.

(usually estimated to be 20–30%), Φ_{PL} is the PLQY of the neat film (59.1% for **3,6-mPPICNC3**, 63.0% for **3,6-pPPICNC3**, 61.9% for **2,7-mPPICNC3** and 63.3% for **2,7-pPPICNC3**). The corresponding EUEs are calculated to be 43.3–64.9%, 32.6–48.9%, 29.0–43.5% and 33.4–50.2% for devices **N1–4**, respectively, which break through the upper limit of 25% in conventional fluorescent OLEDs. The large $\Delta E_{S_1T_1}$ and single-exponential decay lifetime in the nanosecond range of four emitters can rule out the TADF mechanism. Meanwhile, the luminance and current densities of the devices exhibit a good linear relationship (Fig. S19†), confirming that triplet–triplet annihilation (TTA) up-conversion is not the utilization channel of triplet excitons. Combining the analysis of the photophysical properties and theoretical calculations, the HLCT mechanism should be the main reason for their excellent EL efficiencies.

In order to reduce the adverse effects of aggregation, the doped devices(**D1–4**) using 4,4′-bis(*N*-carbazolyl)-1,1′-biphenyl (CBP) as a host for **3,6-mPPICNC3**, **3,6-pPPICNC3**, **2,7-mPPICNC3** and **2,7-pPPICNC3** were prepared with the doping concentration of 5 wt%. As shown in Fig. 7a, b, S20 and S21,† compared to the non-doped OLEDs, devices **D1–4** show obvious blue shifts with emission wavelengths of 391–426 nm and narrow FWHM values, corresponding to the CIE coordinates of (0.161, 0.025), (0.160, 0.035), (0.161, 0.033), and (0.156, 0.063), respectively. Notably, the maximum EQEs of doped devices are improved to be 7.85%, 7.51%, 5.52% and 6.47%. It is especially noteworthy that the **3,6-mPPICNC3**-based device **D1** not only shows stable NUV light with perfect color purity but also achieves a high EQE and minimal efficiency roll-off, maintaining an EQE value of 7.48% at 1000 cd m^{-2}. The J_{90} value of device **D1** can be extracted to be 224 mA cm^{-2}.

Until now, though the record-high EQE of 11.3% has been achieved in doped HLCT-based OLEDs with a CIE*y* value of less than 0.05,[31] most reported devices have exhibited low brightness, serious efficiency roll-off or poor color purity, resulting from unbalanced exciton recombination, exciton quenching effects, strong intramolecular CT state, and aggregation effect, especially in non-doped OLEDs. To the best of our knowledge, **3,6-mPPICNC3**-based non-doped device **N1** achieves an EQE of 7.67% with negligible efficiency roll-off up to a luminance of 3300 cd m^{-2}, which sets a new record among the non-doped NUV-OLEDs with a CIE*y* value of less than 0.05 (Fig. 7c, and Table S11†). In addition, the doped device **D1** shows an EQE of 7.48% at 1000 cd m^{-2} and a narrow FWHM of 41 nm with an emission peak smaller than 400 nm, outperforming most reported doped OLEDs (Fig. 7d, and Table S10†). It is worth emphasizing that our work not only provides an effective design strategy to alleviate the contradictions among the wide-bandgap emission, fluorescence efficiency and aggregation effect, but also realizes balanced bipolar transport and low efficiency roll-off at high brightness through the approach of molecular configuration engineering. In order to further improve the EL efficiencies, it is essential to suppress the competitive intersystem crossing (IC) process from high-lying triplet states to the T_1 state by introducing functional groups (such as anthracene) with a low T_1 energy level.

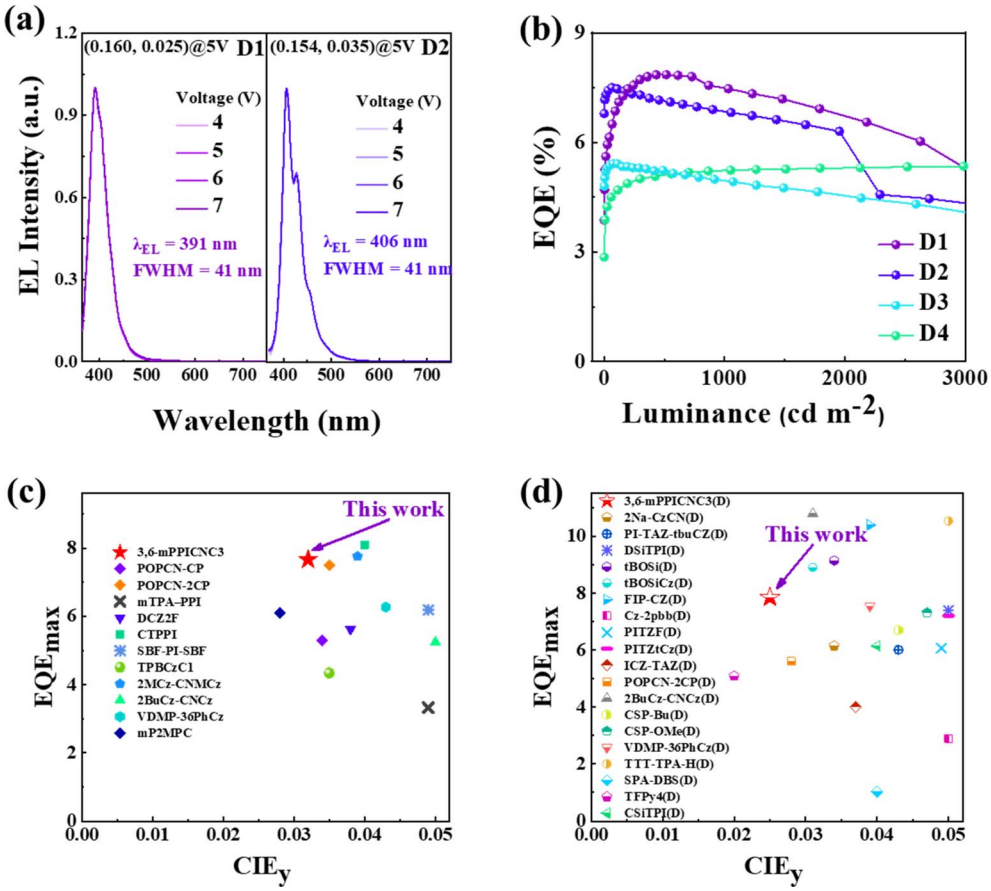

Fig. 7 (a) Normalized EL spectra at different applied voltages of the devices **D1** and **D2**. (b) EQE *versus* luminance curves of the devices **D1–4**. EQE_{max} *versus* CIE*y* of the reported non-doped (c) and doped (d) HLCT-based OLEDs with a CIE*y* value below 0.05.

Conclusion

In summary, four efficient wide-bandgap HLCT emitters, namely **3,6-mPPICNC3**, **3,6-pPPICNC3**, **2,7-mPPICNC3** and **2,7-pPPICNC3**, featuring a unique D′–D–A structure, have been successfully designed and synthesized. It is found that such novel structure endows the emitters with a PLICT character, resulting in high PLQYs in both the solution and neat film. On the other hand, high and balanced bipolar transport was achieved by molecular configuration engineering. As a result, the OLED employing **3,6-mPPICNC3** as an emitter not only achieves stable NUV emission with CIE color coordinates of (0.160, 0.032) and a narrow FWHM of 44 nm, but also exhibits a record-breaking EQE of 7.67% and negligible efficiency roll-off as the luminance increases to 3300 cd m^{-2} in the non-doped device. Furthermore, remarkable EL performance, including an emission peak at 391 nm, a narrow FWHM of 41 nm and a maximum EQE of 7.85%, is achieved simultaneously in the doped device. This work reveals that the D′–D–A type molecular design is a feasible and potentially promising approach to developing efficient and balanced bipolar wide-bandgap emitters and achieving high-performance NUV-OLEDs with high efficiency, low efficiency roll-off, and good color purity.

Data availability

All data supporting the findings of this study are presented in the article and ESI.† Additional data are available from the corresponding author upon reasonable request.

Author contributions

H. Qi, Z. Gao, and S. Wang conducted the synthesis, basic properties characterizations, and theoretical calculations. D. Xie, D. Ma, and S. Ying performed the fabrications and characterization studies of the devices. H. Qi, L. Peng, and Y. Liu, contributed to writing the manuscript, and all the authors revised it. S. Ying, D. Ma, and S. Yan conceived the idea, and supervised this study.

Conflicts of interest

The authors declare that they have no known competing financial interests or personal relationships that could have appeared to influence the work reported in this paper.

Acknowledgements

The authors acknowledge the financial support from the Natural Science Foundation of Qingdao (no. 23-2-1-75-zyyd-jch), the Natural Science Foundation of Shandong Provincial (nos. ZR2023QE078, ZR2022ZD37, and ZR2019ZD50), the National Natural Science Foundation of China (no. 52103220, 52103017, and 22022501), and the Science and Technology Support Plan for Youth Innovation of Colleges and Universities in Shandong Province (2023KJ097).

Notes and references

1 Y. Luo, S. Li, Y. Zhao, C. Li, Z. Pang, Y. Huang, M. Yang, L. Zhou, X. Zheng, X. Pu and Z. Lu, *Adv. Mater.*, 2020, **32**, 2001248.
2 C. Du, H. Liu, Z. Cheng, S. Zhang, Z. Qu, D. Yang, X. Qiao, Z. Zhao and P. Lu, *Adv. Funct. Mater.*, 2023, **33**, 2304854.
3 M. Xie, Y. Zhou, H. Zhou, C. Ma, Q. Sun, S.-T. Zhang, Y. Zhang, W. Yang and S. Xue, *Chem. Sci.*, 2024, **15**, 5589–5595.
4 S. Wang, L. Peng, F. He, Y. Ming, H. Qi, Y. Liu, D. Ma, S. Ying and S. Yan, *Adv. Opt. Mater.*, 2024, **2024**, 2400503.
5 A. Salehi, X. Fu, D. H. Shin and F. So, *Adv. Funct. Mater.*, 2019, **29**, 1808803.
6 M. Du, M. Mai, D. Zhang, L. Duan and Y. Zhang, *Chem. Sci.*, 2024, **15**, 3148–3154.
7 J. Xu, H. Liu, J. Li, Z. Zhao and B. Z. Tang, *Adv. Opt. Mater.*, 2021, **9**, 2001840.
8 J. Wang, Y. Yang, C. Jiang, M. He, C. Yao and J. Zhang, *J. Mater. Chem. C*, 2022, **10**, 3163–3171.
9 X. Guo, P. Yuan, X. Qiao, D. Yang, Y. Dai, Q. Sun, A. Qin, B. Z. Tang and D. Ma, *Adv. Funct. Mater.*, 2020, **30**, 1908704.
10 S. Chen, P. Zeng, W. Wang, X. Wang, Y. Wu, P. Lin and Z. Peng, *J. Mater. Chem. C*, 2019, **7**, 2886–2897.
11 T. C. Chao, Y. T. Lin, C. Y. Yang, T. S. Hung, H. C. Chou, C. C. Wu and K. T. Wong, *Adv. Mater.*, 2005, **17**, 992–996.
12 J. Shinar and R. Shinar, *J. Phys. D: Appl. Phys.*, 2008, **41**, 133001.
13 J. Bian, S. Chen, L. Qiu, N. Zhang, J. Zhang, C. Duan, C. Han and H. Xu, *Research*, 2022, **2022**, 9838120.
14 X. Guo, G. Li, J. Lou, K. Chen, R. Huang, D. Yang, H. Zhang, Z. Wang and B. Z. Tang, *Small*, 2022, **18**, 2204029.
15 S. Zeng, C. Xiao, J. Zhou, Q. Dong, Q. Li, J. Lim, H. Ma, J. Y. Lee, W. Zhu and Y. Wang, *Adv. Funct. Mater.*, 2022, **32**, 2113183.
16 H. Liu, Q. Bai, L. Yao, H. Zhang, H. Xu, S. Zhang, W. Li, Y. Gao, J. Li, P. Lu, H. Wang, B. Yang and Y. Ma, *Chem. Sci.*, 2015, **6**, 3797–3804.
17 Y. Huo, J. Lv, M. Wang, Z. Duan, H. Qi, S. Wang, Y. Liu, L. Peng, S. Ying and S. Yan, *J. Mater. Chem. C*, 2023, **11**, 6347–6353.
18 Z. Zhong, X. Zhu, X. Wang, Y. Zheng, S. Geng, Z. Zhou, X. J. Feng, Z. Zhao and H. Lu, *Adv. Funct. Mater.*, 2022, **32**, 2112969.
19 S. S. Tang, G. X. Yang, J. J. Zhu, X. He, J. X. Jian, F. Lu and Q. X. Tong, *Chem.–Eur. J.*, 2021, **27**, 9102–9111.
20 P. Han, A. Qin and B. Z. Tang, *Chem. Res. Chin. Univ.*, 2021, **37**, 16–24.
21 H. Zhang, G. Li, X. Guo, K. Zhang, B. Zhang, X. Guo, Y. Li, J. Fan, Z. Wang, D. Ma and B. Z. Tang, *Angew. Chem., Int. Ed.*, 2021, **60**, 22241–22247.
22 T. Chen, J. Lou, H. Wu, J. Luo, D. Yang, X. Qiao, H. Zhang, B. Z. Tang and Z. Wang, *Adv. Opt. Mater.*, 2023, **11**, 2301053.
23 G. Li, B. Li, H. Zhang, X. Guo, C. Lin, K. Chen, Z. Wang, D. Ma and B. Z. Tang, *ACS Appl. Mater. Interfaces*, 2022, **14**, 10627–10636.
24 L. Peng, Y. Huo, L. Hua, J. Lv, Y. Liu, S. Ying and S. Yan, *J. Mater. Chem. C*, 2022, **10**, 9621–9627.
25 Y. Zheng, X. Zhu, Z. Ni, X. Wang, Z. Zhong, X. J. Feng, Z. Zhao and H. Lu, *Adv. Opt. Mater.*, 2021, **9**, 2100965.
26 X. Q. Gan, Z. M. Ding, D. H. Liu, W. Q. Zheng, B. Ma, H. Zhang, X. Chang, L. Wang, Y. Liu, X. Wu, S. J. Su and W. Zhu, *Adv. Opt. Mater.*, 2023, **11**, 2300195.
27 S. Geng, Z. Liu, H. Li, Z. Zhong, X. J. Feng, Z. Zhao and H. Lu, *Adv. Opt. Mater.*, 2023, **12**, 2301344.
28 C. Brouillac, W.-S. Shen, J. Rault-Berthelot, O. Jeannin, C. Quinton, Z.-Q. Jiang and C. Poriel, *Mater. Chem. Front.*, 2022, **6**, 1803–1813.
29 P. Ma, Y. Chen, Y. Man, Q. Qi, Y. Guo, H. Wang, Z. Li, P. Chang, C. Qu, C. Han and H. Xu, *Angew. Chem., Int. Ed.*, 2023, **63**, e202316479.
30 Y. Xu, P. Xu, D. Hu and Y. Ma, *Chem. Soc. Rev.*, 2021, **50**, 1030–1069.
31 G. Li, K. Xu, J. Zheng, X. Fang, W. Lou, F. Zhan, C. Deng, Y.-F. Yang, Q. Zhang and Y. She, *J. Am. Chem. Soc.*, 2024, **146**, 1667–1680.
32 H. Zhang, G. Li, X. Guo, K. Zhang, B. Zhang, X. Guo, Y. Li, J. Fan, Z. Wang, D. Ma and B. Z. Tang, *Angew. Chem., Int. Ed.*, 2021, **60**, 22241–22247.
33 J. Chen, H. Liu, J. Guo, J. Wang, N. Qiu, S. Xiao, J. Chi, D. Yang, D. Ma, Z. Zhao and B. Z. Tang, *Angew. Chem., Int. Ed.*, 2022, **61**, e202116810.
34 L. Peng, J. Lv, S. Xiao, Y. Huo, Y. Liu, D. Ma, S. Ying and S. Yan, *Chem. Eng. J.*, 2022, **450**, 138339.
35 P. Han, C. Lin, D. Ma, A. Qin and B. Z. Tang, *ACS Appl. Mater. Interfaces*, 2020, **12**, 46366–46372.
36 A. Obolda, Q. Peng, C. He, T. Zhang, J. Ren, H. Ma, Z. Shuai and F. Li, *Adv. Mater.*, 2016, **28**, 4740–4746.
37 S. Y. Chang, G. T. Lin, Y. C. Cheng, J. J. Huang, C. L. Chang, C. F. Lin, J. H. Lee, T. L. Chiu and M. K. Leung, *ACS Appl. Mater. Interfaces*, 2018, **10**, 42723–42732.
38 H. Lim, H. J. Cheon, S. J. Woo, S. K. Kwon, Y. H. Kim and J. J. Kim, *Adv. Mater.*, 2020, **32**, e2004083.
39 M. Chen, Y. Yuan, J. Zheng, W.-C. Chen, L.-J. Shi, Z.-L. Zhu, F. Lu, Q.-X. Tong, Q.-D. Yang, J. Ye, M.-Y. Chan and C.-S. Lee, *Adv. Opt. Mater.*, 2015, **3**, 1215–1219.
40 C. Li, J. Wei, J. Han, Z. Li, X. Song, Z. Zhang, J. Zhang and Y. Wang, *J. Mater. Chem. C*, 2016, **4**, 10120–10129.
41 H. Wei, R. Zhang, G. Huang, Y. Yuan and W. Chen, *Opt. Mater.*, 2022, **128**, 112345.
42 C. Liao, B. Chen, Q. Xie, X. Li, H. Liu and S. Wang, *Adv. Mater.*, 2023, **35**, 2305310.

43 Y. Huo, J. Lv, Y. Xie, L. Hua, Y. Liu, Z. Ren, T. Li, S. Ying and S. Yan, *ACS Appl. Mater. Interfaces*, 2022, **14**, 57092–57101.
44 Y. Huo, H. Qi, S. He, J. Li, S. Song, J. Lv, Y. Liu, L. Peng, S. Ying and S. Yan, *Aggregate*, 2023, **4**, e391.
45 J. Ye, Z. Chen, M.-K. Fung, C. Zheng, X. Ou, X. Zhang, Y. Yuan and C.-S. Lee, *Chem. Mater.*, 2013, **25**, 2630–2637.
46 X. Yang, S. Zheng, R. Bottger, H. S. Chae, T. Tanaka, S. Li, A. Mochizuki and G. E. Jabbour, *J. Phys. Chem. C*, 2011, **115**, 14347–14352.
47 L. Peng, J. Lv, Y. Huo, L. Hua, Y. Liu, S. Ying and S. Yan, *Dyes Pigm.*, 2022, **206**, 110676.
48 B. Wex and B. R. Kaafarani, *J. Mater. Chem. C*, 2017, **5**, 8622.
49 Z. Wang, T. Yang, S. Dong, Z. Wen, H. Xu, Y. Miao, H. Wang and J. Yu, *Dyes Pigm.*, 2022, **199**, 110047.
50 R. Ma, Z. Ma, X. Wang, Z. Si, Q. Duan and S. Shao, *Chem. Eng. J.*, 2022, **447**, 137517.
51 S. K. Shin, S. Y. Byeon, S. H. Han and J. Y. Lee, *Adv. Opt. Mater.*, 2018, **6**, 1701007.
52 R. K. Konidena, K. R. J. Thomas, A. Pathak, D. K. Dubey, S. Sahoo and J.-H. Jou, *ACS Appl. Mater. Interfaces*, 2018, **10**, 24013–24027.
53 H. Uoyama, K. Goushi, K. Shizu, H. Nomura and C. Adachi, *Nature*, 2012, **492**, 234–238.
54 S. Zhang, L. Yao, Q. Peng, W. Li, Y. Pan, R. Xiao, Y. Gao, C. Gu, Z. Wang, P. Lu, F. Li, S. Su, B. Yang and Y. Ma, *Adv. Funct. Mater.*, 2015, **25**, 1755–1762.
55 S. Ying, W. Liu, L. Peng, Y. Dai, D. Yang, X. Qiao, J. Chen, L. Wang and D. Ma, *Adv. Opt. Mater.*, 2022, **10**, 2101920.
56 R. Guo, W. Liu, S. Ying, Y. Xu, Y. Wen, Y. Wang, D. Hu, X. Qiao, B. Yang, D. Ma and L. Wang, *Sci. Bull.*, 2021, **66**, 2090–2098.
57 X. Tang, Q. Bai, T. Shan, J. Li, Y. Gao, F. Liu, H. Liu, Q. Peng, B. Yang, F. Li and P. Lu, *Adv. Funct. Mater.*, 2018, **28**, 1705813.
58 Y. Xu, X. Liang, X. Zhou, P. Yuan, J. Zhou, C. Wang, B. Li, D. Hu, X. Qiao, X. Jiang, L. Liu, S.-J. Su, D. Ma and Y. Ma, *Adv. Mater.*, 2019, **31**, 1807388.
59 G.-X. Yang, H.-J. Tan, J.-W. Zhao, J.-J. Zhu, X. He, J.-X. Jian, M.-H. Zhou, S.-L. Tao and Q.-X. Tong, *Chem. Eng. J.*, 2022, **445**, 136813.
60 F. Liu, G. Cao, Z. Feng, Z. Cheng, Y. Yan, Y. Xu, Y. Jiang, Y. Chang, Y. Lv and P. Lu, *ACS Appl. Mater. Interfaces*, 2023, **15**, 47307–47316.
61 G. Haberhauer, R. Gleiter and C. Burkhart, *Chem.–Eur. J.*, 2015, **22**, 971–978.
62 G. Haberhauer, *Chem.–Eur. J.*, 2017, **23**, 9288–9296.
63 H. Wu, L. Du, J. Luo, Z. Wang, D. L. Phillips, A. Qin and B. Z. Tang, *J. Mater. Chem. C*, 2022, **10**, 8174–8180.
64 R. Ahmed and A. K. Manna, *J. Phys. Chem. A*, 2022, **126**, 4221–4229.
65 M. A. El-Sayed, *J. Chem. Phys.*, 1963, **38**, 2834–2838.
66 M. K. Etherington, J. Gibson, H. F. Higginbotham, T. J. Penfold and A. P. Monkman, *Nat. Commun.*, 2016, **7**, 13680.
67 Z. Gao, Z. Wang, T. Shan, Y. Liu, F. Shen, Y. Pan, H. Zhang, X. He, P. Lu, B. Yang and Y. Ma, *Org. Electron.*, 2014, **15**, 2667–2676.
68 J. Lou, G. Li, X. Guo, B. Li, D. Yang, H. Zhang, Z. Wang and B. Z. Tang, *Small*, 2023, 202308468.
69 B. Li, J. Lou, H. Zhang, G. Li, X. He, Y. Huang, N. Zheng, Z. Wang, D. Ma and B. Z. Tang, *Adv. Funct. Mater.*, 2023, **33**, 2212876.
70 Y. Liu, X. Man, Q. Bai, H. Liu, P. Liu, Y. Fu, D. Hu, P. Lu and Y. Ma, *CCS Chem.*, 2022, **4**, 214–227.
71 W. Wang, K. Chen, H. Wu, Y. Long, J. Zhao, L. Jiang, S. Liu, Z. Chi, J. Xu and Y. Zhang, *ACS Appl. Mater. Interfaces*, 2023, **15**, 13415–13426.
72 H. Xu, P. Sun, K. Wang, J. Li, F. Wang, Y. Miao, H. Wang, B. Xu and W.-Y. Wong, *J. Mater. Chem. C*, 2017, **5**, 4455–4462.
73 M. Sun, C. Ma, M. Xie, L. Chu, Q. Sun, W. Yang and S. Xue, *Chem. Eng. J.*, 2024, **480**, 148107.
74 J. Lv, S. Song, J. Li, L. Peng, Y. Li, Y. Liu, D. Ma, S. Ying and S. Yan, *Adv. Opt. Mater.*, 2023, **12**, 2301413.